Molecular Plant
Research article

CellPress
Partner Journal

Sucrose-responsive osmoregulation of plant cell size by a long non-coding RNA

Jakub Hajný[1,*], Tereza Trávníčková[1], Martina Špundová[2], Michelle Roenspies[3], R.M. Imtiaz Karim Rony[4], Sebastian Sacharowski[5], Michal Krzyszton[5], David Zalabák[1], Christian S. Hardtke[6], Aleš Pečinka[7], Holger Puchta[3], Szymon Swiezewski[5], Jaimie M. van Norman[4,8] and Ondřej Novák[1]

[1]Laboratory of Growth Regulators, Czech Academy of Sciences, Institute of Experimental Botany and Palacky University, Slechtitelu 27, 77900 Olomouc, Czech Republic

[2]Department of Biophysics, Faculty of Science, Palacky University, Slechtitelu 27, 77900 Olomouc, Czech Republic

[3]Joseph Gottlieb Kölreuter Institute for Plant Sciences (JKIP)–Molecular Biology, Karlsruhe Institute of Technology, 76131 Karlsruhe, Germany

[4]Department of Molecular, Cell, and Systems Biology, University of California, Riverside, CA 92521, USA

[5]Laboratory of Seeds Molecular Biology, Institute of Biochemistry and Biophysics Polish Academy of Sciences, Pawinskiego 5a, 02-106 Warsaw, Poland

[6]Department of Plant Molecular Biology, University of Lausanne, 1015 Lausanne, Switzerland

[7]Center of Plant Structural and Functional Genomics, Institute of Experimental Botany, Czech Academy of Sciences, Šlechtitelů 31, 77900 Olomouc, Czech Republic

[8]Department of Molecular, Cell, and Developmental Biology, University of California, Los Angeles, Los Angeles, CA 90095, USA

***Correspondence: Jakub Hajný (jakub.hajny@upol.cz)**

https://doi.org/10.1016/j.molp.2024.09.011

ABSTRACT

In plants, sugars are the key source of energy and metabolic building blocks. The systemic transport of sugars is essential for plant growth and morphogenesis. Plants evolved intricate molecular networks to effectively distribute sugars. The dynamic distribution of these osmotically active compounds is a handy tool for regulating cell turgor pressure, an instructive force in developmental biology. In this study, we have investigated the molecular mechanism behind the dual role of the receptor-like kinase CANAR. We functionally characterized a long non-coding RNA, *CARMA*, as a negative regulator of CANAR. Sugar-responsive *CARMA* specifically fine-tunes *CANAR* expression in the phloem, the route of sugar transport. Our genetic, molecular, microscopy, and biophysical data suggest that the CARMA–CANAR module controls the shoot-to-root phloem transport of sugars, allows cells to flexibly adapt to the external osmolality by appropriate water uptake, and thus adjust the size of vascular cell types during organ growth and development. Our study identifies a nexus of plant vascular tissue formation with cell internal pressure monitoring, revealing a novel functional aspect of long non-coding RNAs in developmental biology.

Key words: lncRNA, auxin, turgor, sugar transport, cell size

Hajný J., Trávníčková T., Špundová M., Roenspies M., Rony R.M.I.K., Sacharowski S., Krzyszton M., Zalabák D., Hardtke C.S., Pečinka A., Puchta H., Swiezewski S., van Norman J.M., and Novák O. (2024). Sucrose-responsive osmoregulation of plant cell size by a long non-coding RNA. Mol. Plant. **17**, 1719–1732.

INTRODUCTION

In contrast to the circulatory vascular system of vertebrates, plants evolved non-circulatory specialized vascular bundles with two distinct long-distance transport routes. The xylem (X) is a unidirectional root-to-shoot path for the transport of water and minerals from the soil. The phloem route transports carbon assimilates, amino acids, RNAs, and hormones from source tissues (e.g., mature leaves) into sink tissues (such as juvenile leaves, roots, meristems, and reproductive organs) (Fukuda and Ohashi-Ito, 2019; Hardtke, 2023). The hydrostatic pressure differences between source and sink drive the flow of the phloem content (Knoblauch et al., 2016). In most plants, sucrose is the main form of assimilated carbon from photosynthesis, making it the central metabolite in plant growth and development. Sucrose is synthesized from fructose and glucose in photosynthetically active cells. Plants favor non-reducing sugar sucrose since high concentrations of reducing sugars can non-enzymatically

Published by the Molecular Plant Shanghai Editorial Office in association with Cell Press, an imprint of Elsevier Inc., on behalf of CSPB and CEMPS, CAS.

glycosylate essential proteins and interfere with their functionality (Geiger, 2020). In apoplasmically loading plants like *Arabidopsis*, sucrose export from photosynthetic cells (mesophyll in leaves) to the apoplast is facilitated by SUGARS WILL EVENTUALLY BE EXPORTED TRANSPORTERS (SWEET) efflux proteins. Then, sucrose enters the phloem via SUCROSE TRANSPORTERs (SUCs), a process termed apoplastic phloem loading. SUCs are H^+/sucrose symporters, loading sucrose against its concentration gradient. Sucrose is unloaded from the phloem in sink tissues and distributed via SWEET proteins. Sink tissues either store sucrose in vacuoles or convert it back to glucose and fructose by invertase enzymes. Ultimately, the sugars are consumed or stored in vacuoles (Julius et al., 2017; Geiger, 2020).

Plant growth involves physical remodeling of cell-wall mechanics and cell hydrostatic pressure. Plant cells have a high intracellular hydrostatic pressure, called turgor pressure, which results from water uptake in response to the solute concentration (e.g., ions and sugars) and is counterbalanced by the rigid yet dynamic cell walls (Cosgrove, 2016; Ali et al., 2023). If osmotic conditions change, plant cells regulate water and ion transport across the plasma membrane (PM) and remodel their cell wall to compensate for the turgor pressure difference. The balance between turgor pressure and cell-wall tension at the cell level translates to the tissue level, driving tissue patterning. These mechanical forces play an instructive role in developmental biology across kingdoms. For example, accumulating evidence suggests that in the shoot, the epidermis possesses thicker cell walls, providing a high-resistance pillar for aerial organ development. In the root, the endodermis likely plays a role similar to that of the epidermis in the shoot. Both internal turgor pressure and external mechanical perturbations can alter cell size, geometry, polarity, and cell division plane orientation and, thus, finally shape the plant body (Hamant and Haswell, 2017).

In the *Arabidopsis thaliana* root, INFLORESCENCE AND ROOT APICES RECEPTOR KINASE (IRK), a leucine-rich-repeat receptor-like kinase, regulates stele (i.e., the vascular cylinder surrounded by the pericycle layer) size and restricts excessive endodermal cell divisions (Campos et al., 2020). IRK's closest homolog, PXY/TDR-CORRELATED 2 (PXC2), also called CANALIZATION-RELATED RECEPTOR-LIKE KINASE (CANAR), exerts an overlapping, partially redundant function despite not being expressed in the same tissues (Goff et al., 2023). Both IRK and CANAR/PXC2 were recently reported to contribute to vascular patterning via auxin canalization (Hajný et al., 2020; Goff et al., 2023). Interestingly, the relative numbers of cells in the stele between wild-type (WT) and *CANAR* mutant/overexpresser lines are similar despite the significant change in root stele area (Goff et al., 2023). This suggests mechanical remodeling, which, ultimately, alters cell volume instead of cell number. How CANAR participates in cell volume adjustment remains unknown. We propose that the missing link is the fine-tuning of systemic sugar transport.

Long non-coding RNAs (lncRNAs) are essential regulatory elements of eukaryotic transcriptomes. LncRNAs are versatile regulators of gene expression, functioning at different cellular levels, often providing adaptive mechanisms to various stimuli (Wang and Chang, 2011). Only a handful of lncRNAs have been functionally characterized and implicated in aspects of plant development (Chorostecki et al., 2023). In this study, we characterize a newly annotated lncRNA, *CARMA* (*CANAR MODULATOR IN PROTOPHLOEM*), which is located in the proximal promoter region of *CANAR* in the *A. thaliana* genome. *CARMA* fine-tunes the phloem-specific expression of *CANAR* in response to sucrose availability. Tightly controlled *CANAR* levels in the phloem are required for optimal shoot-to-root sugar transport to adjust cell turgor and, thus, stele cell size in response to the environment.

RESULTS

Newly annotated antisense lncRNA is located in the *CANAR* proximal promoter

We set out to unravel the molecular mechanisms regulating CANAR activity by reexamining its expression pattern. Previously, the transcriptional reporter, consisting of the entire intergenic region (4.7 kb) upstream of the *CANAR* start codon with an endoplasmic reticulum-targeted green fluorescent protein (GFP) (*pCANAR::erGFP*), showed weak activity in the *Arabidopsis* root tip (Goff et al., 2023). To observe a more native expression pattern, we rebuilt the reporter by adding the 3′ untranslated region (UTR) downstream of the *CANAR* stop codon to nuclear-targeted GFP and β-glucuronidase (*pCANAR::NLS-GFP-GUS-ter*). This reporter exhibited a markedly stronger fluorescent signal, localized mainly to the lateral root cap and X, corresponding to the previous report (Goff et al., 2023). Lower expression could also be seen in the root phloem precursors: developing protophloem sieve elements (PPh) and metaphloem (MPh) (Figure 1A). β-glucuronidase staining recapitulated previous observations (Wang et al., 2013), showing expression throughout the seedling vasculature. Staining in the first leaves occurred at the position of the future vasculature strands (Figure 1B), supporting the previously described role of CANAR in vascular patterning via auxin canalization (Hajný et al., 2020). We attribute the stronger expression of the novel reporter to the presence of the 3′ UTR, possibly stabilizing the *CANAR* transcripts.

During the design of the *pCANAR* reporter, we noticed a newly annotated 353 bp antisense lncRNA (AT5G00810) in the proximal promoter region of *CANAR*, partially overlapping its 5′ UTR (Figure 1C). We hypothesized that this lncRNA, named *CARMA* (*CANAR MODULATOR IN PROTOPHLOEM*), might help us understand the relationship between tissue-specific expression of *CANAR* and its developmental functions. Using a semi-quantitative RT-PCR, we confirmed that *CARMA* is expressed in seedlings and that the transcript is presumably polyadenylated, as it could be amplified from oligo(dT)-primed cDNA (Figure 1D). We performed 5′ and 3′ rapid amplification of cDNA ends (RACE) to define the full-length *CARMA* transcript. The transcription start site largely matched annotation, whereas the 3′ end had several transcription termination sites. The annotated length of 353 bp constituted ∼50% of all *CARMA* transcripts, with a maximum detected transcript length of 491 bp (Supplemental Figure S1A and S1B).

A transcriptional reporter containing 5 kb upstream of *CARMA* fused with *NLS-GFP-GUS* (*pCARMA(5kb)::NLS-GFP-GUS*) revealed *CARMA* promoter activity in the PPh with occasional expression in MPh. In addition, in the meristematic zone, a shootward gradient of weaker expression in the X was also observed

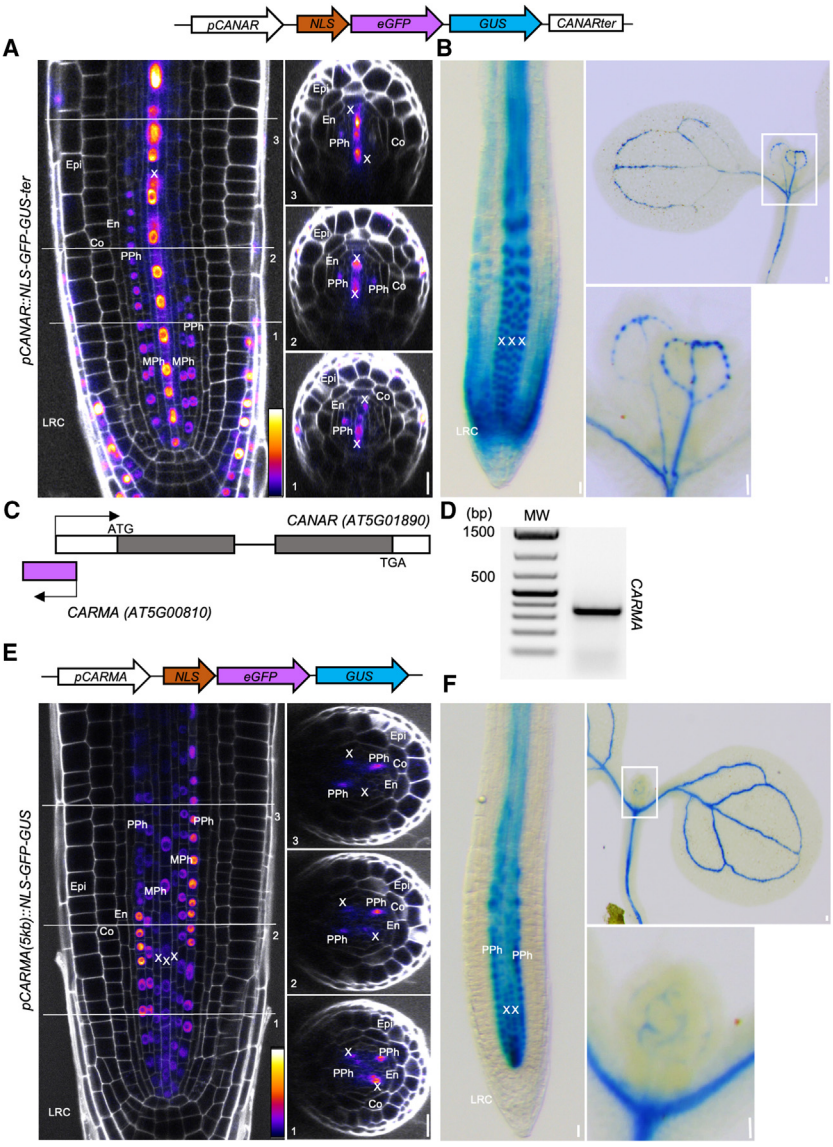

Figure 1. *CARMA* shows a complementary expression pattern with *CANAR* in root protophloem.

(A) Confocal images of a primary root stained with propidium iodide (gray) expressing *pCANAR::NLS-GFP-GUS-ter* (schematic depicted above the images) show *pCANAR* activity in xylem (X), developing protophloem sieve elements (PPh), and lateral root cap (LRC) and weaker expression in metaphloem precursors (MPh).

(B) *pCANAR* activity in roots (left) and cotyledons and true leaves (right, inset) visualized by β-glucuronidase (GUS) staining (blue).

(C) A graphical representation of the *CARMA–CANAR* genomic locus.

(D) Semi-quantitative RT-PCR of *CARMA* RNA from 5-day-old seedlings.

(E) Confocal images of a primary root stained with propidium iodide (gray) expressing *pCARMA(5kb)::NLS-GFP-GUS* (depicted above the images) showing *pCARMA* activity predominantly in PPh with weaker activity in MPh and X.

(F) *pCARMA* activity in roots (left) and cotyledons and true leaves visualized by GUS staining (blue). Numbers in medial longitudinal confocal images represent the position of the transverse optical section taken from a z stack. For each reporter, ≥10 roots were examined. Scale bars, 20 μm. Other cell types: Epi, epidermis; Co, cortex; En, endodermis. See also Supplemental Figure 1.

(Figure 1E and 1F and Supplemental Figure 1C). The activity of *pCARMA* in the X was not seen with a shortened version of the promoter (*pCARMA(1.3kb)::NLS-GFP-GUS*) (Supplemental Figure 1D and 1E). Similar to *pCANAR*, *pCARMA* activity in the first leaves occurred at the position of the future vasculature strands, a manifestation of auxin canalization (Scarpella et al., 2006) (Figure 1F). Thus, *pCANAR* and *pCARMA* have overlapping patterns of activity, but their intensity profiles are inverse, suggesting a possible role for *CARMA* in the transcriptional regulation of *CANAR*.

CARMA controls leaf vascular patterning

CARMA expression in the cotyledons and first leaves prompted us to test the involvement of *CARMA* in leaf vascular patterning, a proxy for auxin canalization (Scarpella et al., 2006). We isolated an available transfer DNA (T-DNA) insertion loss-of-function mutant (*carma-1*) (Supplemental Figure 2A and 2B). Because the *carma-1* T-DNA insertion is close to the *CANAR* 5′ UTR (Supplemental Figure 2A), we tested whether it affects *CANAR* transcription. *CANAR* mRNA levels were slightly elevated (Supplemental Figure 2C), excluding the possibility of T-DNA-mediated knockdown of *CANAR*. Next, we generated transgenic lines overexpressing *CARMA* under the control of the constitutive cauliflower mosaic virus *35S* promoter (Supplemental Figure 2D). Two independent *35S::CARMA* overexpression lines showed a higher incidence of extra vascular loops, extra branches, and disconnections in the upper loops compared to the WT (Columbia-0 [Col-0]) control (Figure 2A and 2B). These higher-complexity venation phenotypes resembled those of *canar* mutants (Hajný et al., 2020). In contrast, *carma-1* plants exhibited simpler venation, indicated by missing loops (Figure 2C and 2D), similar to *35S::CANAR-GFP* (Hajný et al., 2020). The inverse intensity of *pCANAR* and *pCARMA* activity in the X/PPh and the opposite vein patterning phenotypes indicate that *CARMA* is a negative regulator of *CANAR* activity.

CARMA mediates cell-size changes in response to medium osmolality in the stele

Whereas *canar-3* roots had an enlarged stele area, *CANAR* overexpression had the opposite effect. The stele area difference was due to a change in cell size and not cell number. This phenotype was conditional, manifested only in more hypotonic growth conditions where the agar plates contained 0.2× strength Murashige and Skoog (MS) basal salts medium (Goff et al., 2023), suggesting an involvement of internal water pressure in the *CANAR* phenotype. Thus, we tested whether *CARMA* also plays a role in stele area control on medium with different osmolalities (0.2×, 0.5×, and 1× MS).

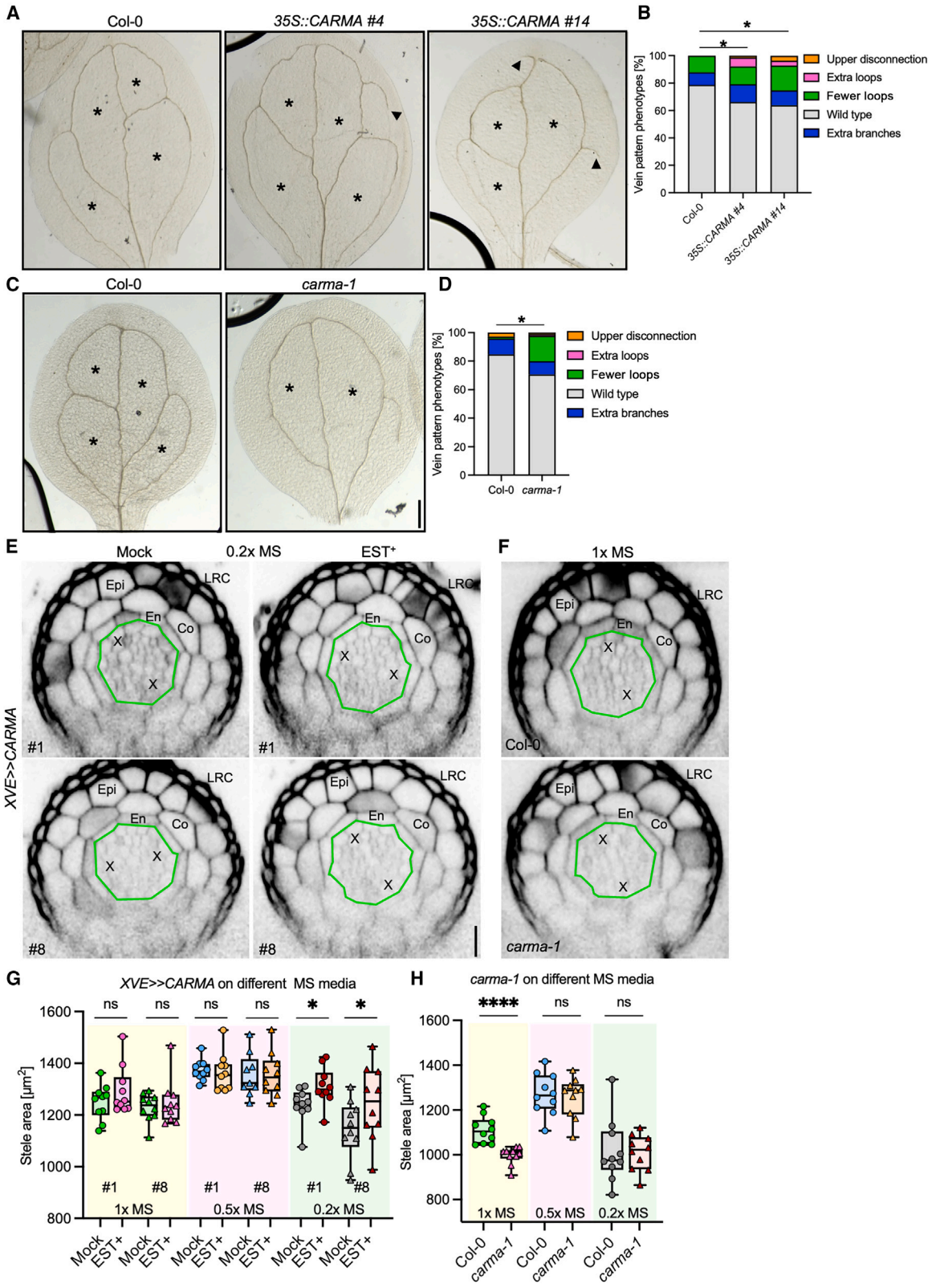

Figure 2. *CARMA* regulates leaf vascular patterning and root stele area.

(A and C) Representative images of cotyledon vasculature from 10-day-old Col-0, two independent *35S::CARMA* transgenic lines, and *carma-1* seedlings. Black asterisks mark a number of closed loops. Black arrowheads highlight extra branches. Scale bar, 100 μm.

(legend continued on next page)

As *35S* promoter activity is weak in the root meristem vasculature, we overexpressed *CARMA* under the β-estradiol-inducible promoter (Zuo et al., 2000) (*XVE>>CARMA*) (Supplemental Figure 2E). After β-estradiol treatment from germination onward, we observed a significantly enlarged stele area on 0.2× MS in two independent *XVE>>CARMA* lines compared to the mock controls Figure 2E and 2G), similar to what has been observed for *canar* mutants (Goff et al., 2023). Conversely, the *carma-1* roots exhibited a smaller stele area than WT, but only on 1× MS medium (Figure 2F and 2H), analogous to but weaker than the *XVE>>CANAR* overexpression stele phenotype (Goff et al., 2023). Again, no change in the vascular cell number was observed (Supplemental Figures 2G, 2H, 3A, and 3B), indicating the difference in stele area can be attributed to altered cell size, not proliferation. By measuring the distance from the endodermis to the lateral root cap, we confirmed that cell expansion is specific to the stele (Supplemental Figures 2F and 3C). Also, no change in root meristem length was observed (Supplemental Figures 2I, 2J, 3D, and 3E), indicating that the stele area phenotype is not the result of changes in differentiation.

To this end, our results suggest that *CARMA* is a negative regulator of *CANAR.* A cross of the *canar-3* mutant with the *XVE>>CARMA* overexpressing line could not further enhance the *canar-3* stele area phenotype on 0.2× MS medium (Supplemental Figure 2K), proving that *CANAR* is a primary target of *CARMA*. Given the close proximity of the T-DNA cassette of *carma-1* and *canar-3* mutants, a successful generation of a double mutant via crossing is not possible. Hence, we opted for CRISPR-Cas9-mediated deletion of the *CARMA* locus and part of the first exon of *CANAR* (Supplemental Figure 3F and 3G). We obtained two independent lines, which we named *canar-4 C2* and *canar-4 C4*. Both mutants showed no rescue on 0.2× MS, placing *CARMA* upstream of the CANAR function (Supplemental Figure 2L).

The conditional nature of these stele area phenotypes indicates a dependence on the osmolality of the medium. Because the *canar-3* mutant has an enlarged stele on hypotonic medium, we hypothesized that stele cells might retain excess water, making them bulkier. If true, lowering the intracellular water content would revert the phenotype. To test this hypothesis, we decided to use mannitol, an osmotically active sugar that cannot penetrate the PM (Hohl and Schopfer, 1991) and, therefore, reduce cellular water content. To isolate the effect of osmolality from other effects, such as nutrient level, we measured the osmolality of 0.2× MS (29 mOsm/kg) and 1× MS (95 mOsm/kg) media and then supplemented 0.2× MS medium with mannitol to match the osmolality of 1× MS (Supplemental Table 1). The needed mannitol concentration was approximately 64 mM. Indeed, the *canar-3* mutant phenotype was reverted on 0.2× MS medium with 64 mM mannitol (Supplemental Figure 2M). A similar effect was observed for *XVE>>CARMA* (Supplemental Figure 2N), while Col-0 could compensate for the osmolality change normally (Supplemental Figure 2O).

CARMA fine-tunes *CANAR* expression in the root protophloem

The antisense orientation of *CARMA*, its inverse intensity expression profile in the X/PPh, and its opposite leaf vasculature and stele area phenotypes with respect to *CANAR* imply that *CARMA* is a negative regulator of *CANAR*. To understand how *CARMA* influences CANAR function, we generated a set of transcriptional reporters consisting of the full-length 4.7 kb *CANAR* promoter, *pCANAR::NLS-GFP-GUS-ter*; a partial deletion of *CARMA*, *pCANAR_CARMAΔ::NLS-GFP-GUS-ter*; and a complete deletion of *CARMA* (removing part of the *CANAR* 5′ UTR as well), *pCANAR_CARMAΔΔ::NLS-GFP-GUS-ter* (Figure 3A), transformed into the *carma-1* mutant background. Using confocal microscopy, we observed that both deletions resulted in a significant, tissue-specific increase in *pCANAR* activity in the PPh to a level comparable to X. The insertional character of these transgenic lines does not allow absolute quantification; therefore, we opted for relative quantification of the PPh/X ratio of the fluorescence signal. Two independent transgenic lines were analyzed for each reporter (Figure 3A and 3B and Supplemental Figure 4A and 4B). The similar outcomes of the *CARMA*Δ and *CARMA*ΔΔ deletions confirmed that changes in *pCANAR* activity are not due to an indirect impact of its partial 5′ UTR deletion. In line with our observations, the *carma-1* mutant had increased (Supplemental Figure 2C) and *35S::CARMA* overexpression decreased *CANAR* levels (Supplemental Figure 4C). Modest changes in *CANAR* expression reflect a smaller pool of protophloem cells compared to that of the X.

Our results have demonstrated that *CARMA* modulates *CANAR* levels to establish a differential of high *CANAR* expression in the X and low in the PPh. To address the biological significance of this stringent PPh-specific fine-tuning mechanism, we expressed *CANAR* either ubiquitously or tissue specifically in the PPh. We utilized an *XVE>>CANAR-3xHA* line, which inducibly overexpresses *CANAR*, causing a marked decrease in the stele area (Goff et al., 2023). We could elicit this phenotype on 1× MS medium (Figure 3C and 3D), where the *carma-1* plants exhibited a smaller stele area as well (Figure 2F and 2H). Next, we generated *pCVP2>>XVE::CANAR-GFP-ter*, allowing for protophloem-specific inducible overexpression of *CANAR* (Fandino et al., 2023). These transgenic plants grown on β-estradiol showed

(B and D) Quantification of observed vein pattern phenotypes as a percentage. For each genotype, ≥66 cotyledons were analyzed. Student's *t*-test compared the overall incidence of tested defects in marked datasets (*$P < 0.05$).

(E) Transverse optical sections of 5-day-old root meristems stained with propidium iodide (black) from two independent inducible CARMA overexpression (*XVE>>CARMA*) lines (#1 and #8) on 0.2× MS medium with 5 μM (EST^+) and without (mock) β-estradiol. Scale bar, 20 μm.

(F) Transverse optical sections of 5-day-old root meristems stained with propidium iodide of Col-0 and *carma-1* mutant on 1× MS. Green line indicates the measured stele area for **(G)** and **(H)**.

(G and H) Boxplots showing stele area quantification of *XVE>>CARMA* and *carma-1* on different concentrations of MS medium. Whiskers indicate max/min, box shows the interquartile range, with a black line showing the median. Colored symbols are measurements from individual roots. The experiments were carried out three times (8–10 roots for each genotype per replicate); one representative biological replicate is shown. A one-way ANOVA compared marked datasets (*$P < 0.05$ and ****$P < 0.0001$). Cell types: Epi, epidermis; Co, cortex; En, endodermis; X, xylem; LRC, lateral root cap. The transverse optical sections were taken approximately 100 μm from QC (quiescent center). See also Supplemental Figures 2 and 3.

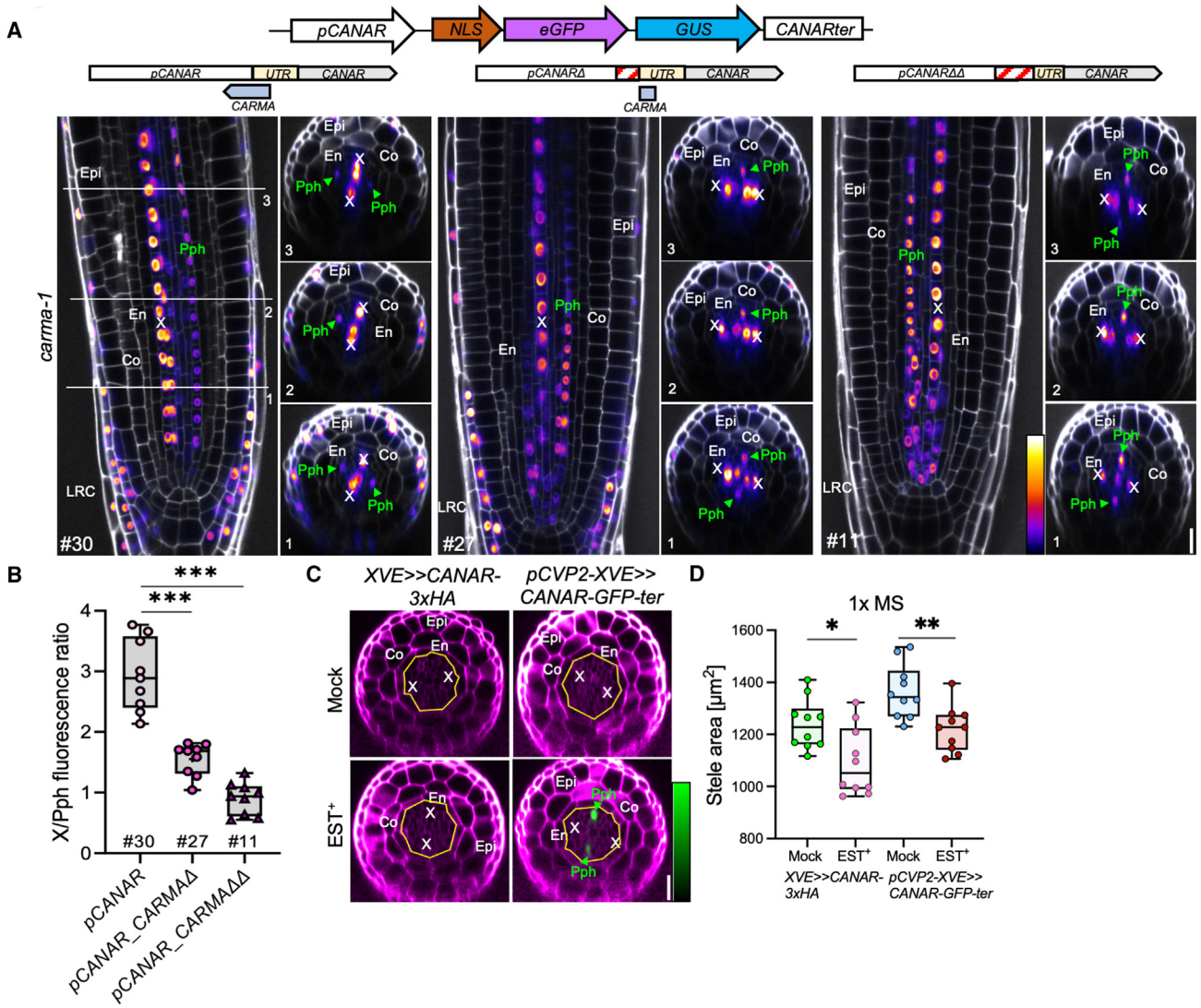

Figure 3. *CARMA* fine-tunes protophloem-specific expression of *CANAR*.

(A) Representative confocal images of primary roots, stained with propidium iodide (white), of *carma-1* plants expressing *pCANAR::NLS-GFP-GUS-ter*, *pCANAR_CARMAΔ::NLS-GFP-GUS-ter*, or *pCANAR_CARMAΔΔ::NLS-GFP-GUS-ter* reporters (schematics shown above images). #30, #27, and #11 mark particular independent transgenic lines. Both partial and complete deletion of *CARMA* led to increased *pCANAR* activity in the PPh (highlighted with a green label and arrowhead). Numbers represent the position of a transverse optical section taken from z stacks.

(B) Boxplot showing relative fluorescence of reporters in **(A)**, where the signal in the PPh is normalized to that in the X (see the methods for details). Whiskers indicate the max/min, the box shows the interquartile range, and the median is shown with a black line. Colored symbols show measurements for individual roots.

(C) Transverse optical sections of 5-day-old root meristems stained with propidium iodide (magenta) from plants expressing *XVE>>CANARx3HA* and *pCVP2>>CANAR-GFP-ter* grown on 1× MS medium with (EST$^+$) and without (mock) β-estradiol from the time of germination. The outer edge of the stele is indicated by the yellow line.

(D) Boxplot showing stele area quantification of the plants in **(C)**. Whiskers indicate the max/min, the box shows an interquartile range, and the median is shown with a black line. Colored symbols are measurements from individual roots. These experiments were done three times (8–10 roots for each genotype per experiment); one representative biological replicate is shown. A one-way ANOVA compared marked datasets (*$P < 0.05$, **$P < 0.01$, and ***$P < 0.001$). Scale bars, 20 μm. Cell types: Epi, epidermis; Co, cortex; En, endodermis; PPh, developing protophloem sieve elements; X, xylem; and LRC, lateral root cap. See also Supplemental Figure 4.

protophloem-specific GFP fluorescence (Figure 3C) and had significantly decreased stele area, although not to the extent of *XVE>>CANAR-3xHA* (Figure 3D). This effect was not observed on 0.5× and 0.2× media, although *XVE>>CANAR-3xHA* had variable stele area on 0.2× MS medium without a reproducible trend across all replicates (Supplemental Figure 4D and 4E). This could mean that either the X-expressed *CANAR* is also involved in this process or it is a consequence of *CANAR* misexpression. Alternatively, the phenotypic difference might be due to the missing *CANAR* expression in MPh when the *CVP2* (*COTYLEDON VASCULAR PATTERN 2*) promoter is used. These results suggest that fine-tuned levels of *CANAR* in the PPh are

required for the cell-size adjustment in response to changes in external osmolality and are, thus, required for the optimization of stele area.

CARMA mediates *CANAR* responsivity to sucrose

To better understand the CANAR function, we set out to analyze the translational fusion of CANAR driven by its native promoter (*pCANAR::CANAR-GFP*) (Goff et al., 2023). Since the expression was too weak, we deployed an approach similar to that with the *pCANAR::NLS-GFP-GUS-ter* transcriptional reporter, where the addition of the *CANAR* 3′ UTR enhanced the fluorescence signal. Indeed, *pCANAR::CANAR-GFP-ter* provided a stronger signal (Supplemental Figure 5A). Except for the PM, a vesicular signal in the cytoplasm could also be observed, suggesting dynamic subcellular trafficking of CANAR. We noticed that fluorescence intensity and PM-localized signal in two independent transgenic lines depended on the presence of sucrose in the growth medium (Supplemental Figure 5A). Glucose exerted a similar effect, which was not observed after treatment with mannitol (Figure 4A and Supplemental Figure 5B) or NaCl (Supplemental Figure 5C) or by changing the medium osmolality (0.2×, 0.5×, and 1× MS) (Supplemental Figure 5D). Three-fold higher sucrose concentration did not stimulate additional accumulation of CANAR (Figure 4A and Supplemental Figure 5B), indicating a maximum threshold. To further uncouple the effect of sugar from the osmotic pressure, we tested if sucrose-mediated CANAR upregulation can be rescued by a cotreatment with mannitol, which should compete with sucrose for intracellular water and thus alleviate the internal pressure. Mannitol did not change the sucrose responsivity of CANAR (Figure 4A and Supplemental Figure 5B). The same observations were also made for the *pCARMA(5kb)::NLS-GFP-GUS* transgenic line (Supplemental Figure 6A).

Next, we tested if CANAR expression in the root could respond to sugars transported from the shoot. Plants were grown on 0.5× MS medium without sucrose for 5 days, and then the shoots were placed on a glass cover lid to separate them from the medium. Shoots were exposed to liquid 0.5× MS medium alone or containing sucrose or glucose. After 5 h, we observed CANAR upregulation in the root upon sucrose and glucose application (Figure 4B and 4C).

Increased CANAR accumulation in the root upon exposure to sucrose is, at least partially, explained by increased *CANAR* mRNA levels in both leaves and roots (Figure 4D and 4E). In leaves, *CANAR* response was transient, peaking at 0.5–1 h, and then it was gradually lost. In roots, sucrose-mediated *CANAR* upregulation peaked at 2 h, and then it slightly decreased to levels maintained throughout the tested time window. *CARMA* followed a similar trend in both tissues (Figure 4D and 4E). In the *carma-1* mutant, *CANAR* sensitivity to sucrose was elevated in both leaves and roots (Figure 4F and 4G), whereas overexpression of *CARMA* did not show any effect in the tested conditions (Figure 4H and 4I). Mannitol did not affect *CARMA* or *CANAR* expression (Supplemental Figure 5E and 5F).

In summary, sucrose upregulates both *CANAR* and *CARMA* expression in similar temporal manners. The upregulation is specific to PM-permeative sugars, since using other osmotically active molecules did not mimic this effect. *CARMA* changes the *CANAR* sensitivity to sucrose.

The CARMA–CANAR module regulates the shoot-to-root transport of sugars

The upregulation of CANAR in response to sugars led us to hypothesize that CANAR may regulate sugar distribution. Notably, inducing *CANAR* overexpression in *XVE>>CANAR-3xHA* seedlings by growing them on 0.5× MS medium with β-estradiol strongly reduced growth (Supplemental Figure 6H and 6J). This pleiotropic phenotype is reminiscent of various sugar transporter mutants or overexpression lines (Xue et al., 2022). This phenotype was partially rescued by external sucrose application (Supplemental Figure 6I and 6K). Therefore, we examined the expression of sugar transporters in plants overexpressing *CANAR*. SWEETs have been most extensively characterized in *A. thaliana*, which contains four SWEET clades: I and II for final distribution of sucrose, glucose, and fructose within sink tissues; III for phloem loading and unloading; and IV for vacuolar sugar storage (Xue et al., 2022). In addition, the *Arabidopsis* genome encodes nine SUC transporters (SUC1–9) (Bavnhøj et al., 2023). We selected *SWEET11/12*, which are expressed in leaf phloem parenchyma cells and affect vascular development (Le Hir et al., 2015), and *SWEET16/17*, which function in root vacuolar storage of glucose and fructose (Guo et al., 2014). For the *SUCs*, we chose *SUC1/2/3/4*, which are expressed in the shoot and root, with SUC2 being the main contributor to shoot-to-root sucrose transport (Durand et al., 2018). We induced *CANAR* expression overnight to allow for sufficient protein translation while avoiding secondary effects from prolonged treatment. All tested *SWEETs*, except *SWEET12*, were strongly downregulated (Supplemental Figure 6B). *SUC1* and *SUC2* were downregulated as well, while *SUC3* was upregulated (Supplemental Figure 6C). In a complementary experiment, we tested *SWEET* and *SUC* expression in the *canar-3 irk-4* double mutant. We found that *SWEET11* and *SWEET16* were downregulated, and *SUC1* was slightly upregulated (Supplemental Figure 6D and 6E). Except for a modest change in *SUC2*, we did not observe any pronounced effect in the *canar-3* single mutant (Supplemental Figure 6F and 6G), which aligns with its reported redundancy with IRK (Goff et al., 2023). Moreover, tissue-specific effects may be concealed due to the inherently low resolution of RT-qPCR using whole seedlings.

These results indicate that sugar transporters are downstream of the CARMA-CANAR module activity. We utilized a widely used phloem-mobile probe, 5-carboxyfluorescein diacetate (CFDA), to substantiate our hypothesis further. When applied to leaves, CFDA is cleaved by endogenous esterases to produce a fluorescent dye. The dye is transported to sink tissues where it can be visualized (Ross-Elliott et al., 2017). We applied CFDA to leaves of Col-0, *canar-3*, *canar-3 irk-4*, and *XVE>>CANAR-3xHA*, and after 45 min, we analyzed CFDA accumulation in root meristem using confocal microscopy. We saw an increased accumulation of CFDA in *canar-3 irk-4* compared to Col-0, suggesting a higher content of osmotically active sugars in the root meristem. Conversely, the majority of *XVE>>CANAR-3xHA* roots after induction did not exhibit any staining (Figure 5A and 5B),

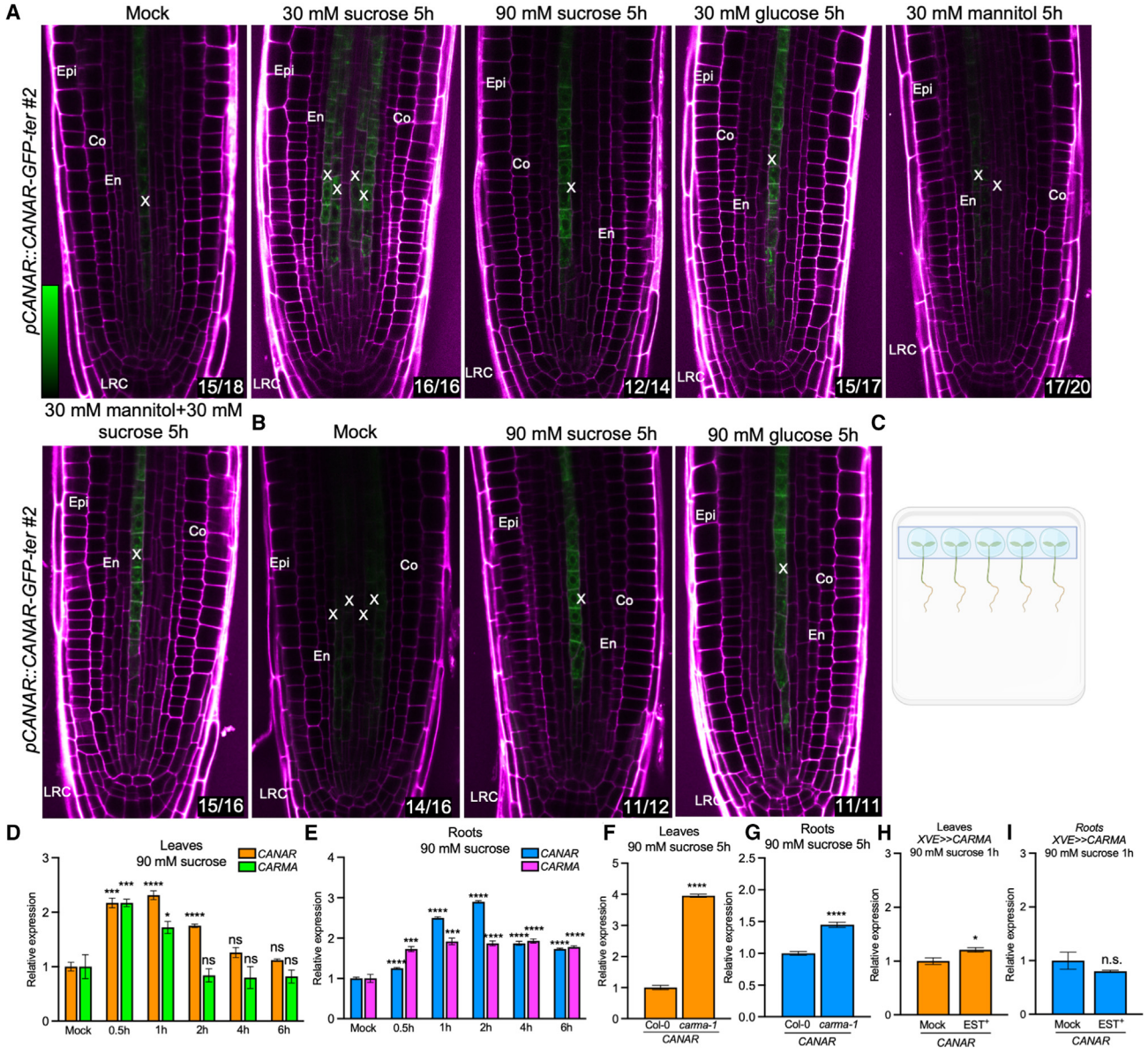

Figure 4. *CARMA* mediates the sugar responsiveness of CANAR.

(A) Representative confocal images of primary roots grown on 0.5× MS medium, stained with propidium iodide (magenta), expressing *pCANAR::CANAR-GFP-ter* #2 and treated 5 h in liquid 0.5× MS medium with mock, 30 mM sucrose, 90 mM sucrose, 30 mM glucose, 30 mM mannitol, or 30 mM sucrose +30 mM mannitol. The dark, non-fluorescent structure in the xylem cells is the nucleus. After 5 h, root meristems were imaged. For each treatment, ≥12 roots were analyzed, and the images were acquired using comparable settings. Scale bar, 20 μm. Cell types: Epi, epidermis; Co, cortex; En, endodermis; X, xylem; and LRC, lateral root cap. White numbers at the bottom right corner indicate the frequency of observed expression pattern.

(B and C) Representative confocal images of primary roots grown on 0.5× MS medium, stained with propidium iodide (magenta), expressing *pCANAR::CANAR-GFP-ter 2*. After 5 days, shoots were placed on a glass cover lid, and droplets of liquid 0.5× MS medium containing mock, 90 mM sucrose, or 90 mM glucose were applied to the shoots **(C)**.

(D–I) Relative expression by RT-qPCR of *CARMA* and *CANAR* after spraying with 90 mM sucrose on 0.5× MS in **(D)** leaves and **(E)** roots. Relative expression by RT-qPCR of *CANAR* in Col-0 and *carma-1* after spraying with 90 mM sucrose in 0.5× MS in **(F)** leaves and **(G)** roots. Relative expression by RT-qPCR of *CANAR* in *XVE>>CARMA* grown on mock or EST^{+} after spraying with 90 mM sucrose in 0.5× MS in **(H)** leaves and **(I)** roots. The graphs represent three biological replicates. Error bars represent SE. A one-way ANOVA compared marked datasets (*$P < 0.05$, **$P < 0.01$, ***$P < 0.001$, and ****$P < 0.0001$). See also Supplemental Figures 5 and 6.

evidencing a lower content of sugars. No reproducible differences were observed for *canar-3*, *carma-1*, or *XVE>>CARMA* lines (Figure 5A and 5B and Supplemental Figure 7A and 7B), which is most likely due to their weaker stele area phenotype, in contrast to *canar-3 irk-4* and *XVE>>CANAR-3xHA* (Goff et al., 2023), and the low resolution of the CFDA approach.

The expected higher sugar content in the roots should be accompanied by a decrease in root osmotic potential, promoting water

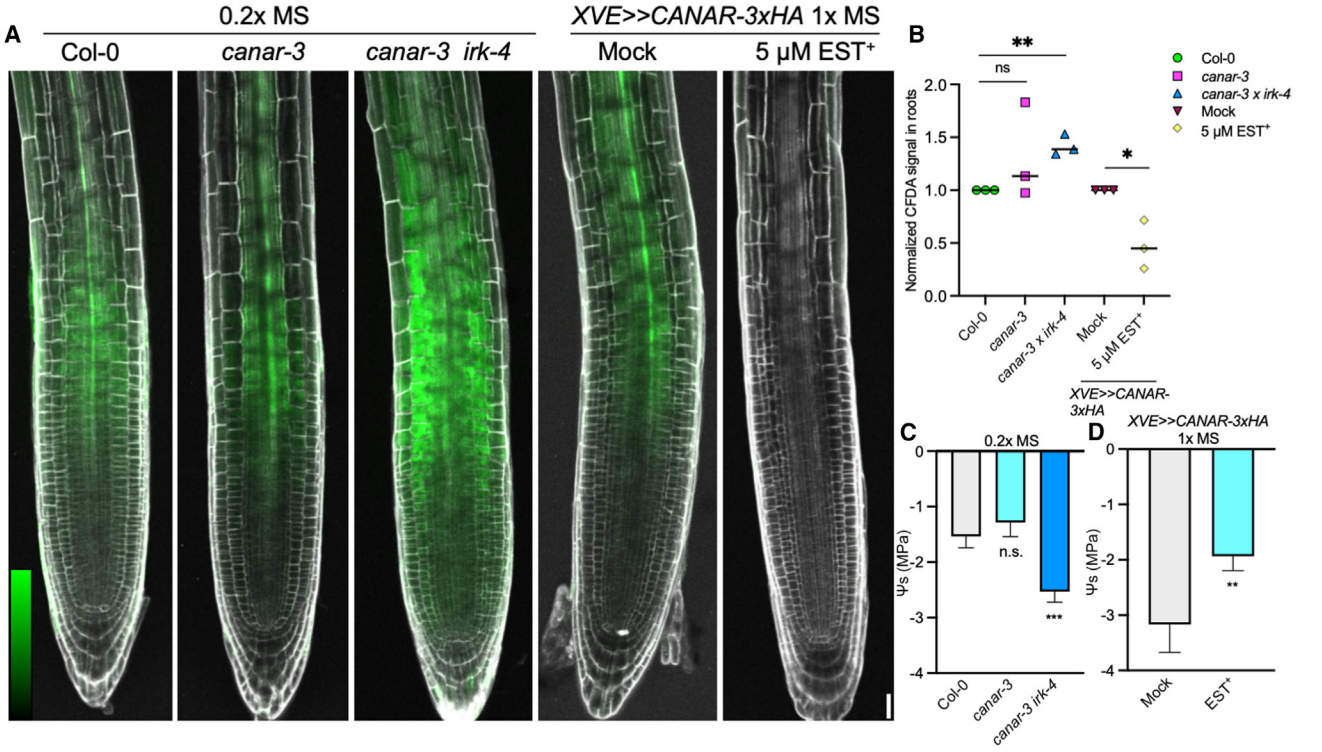

Figure 5. CANAR regulates the shoot-to-root phloem transport of osmotically active compounds.

(A and B) Representative images of 5-day-old seedlings grown on 0.2× MS for Col-0, *canar-3*, and *canar-3 irk-4* and on 1× MS with (EST^+) or without β-estradiol (mock) for *XVE>>CANAR-3xHA*. Shoots were placed on a glass cover lid, and a 2 μl droplet of 1 mM CFDA in water was placed on each shoot. After 45 min, the seedlings were placed on an agar block stained with propidium iodide (gray) and imaged. Scale bar, 20 μm. **(B)** Quantification of **(A)** by measuring the fluorescence intensity of CFDA in roots. Each colored symbol represents one biological experiment where fluorescence intensity in approximately 20 roots grown on one agar plate was measured and averaged. The average values were normalized to respective control. The median is shown with a black line. Three biological replicates were done for each genotype/treatment. Student's *t* test compared marked datasets ($^*P < 0.05$ and $^{**}P < 0.01$).

(C and D) Quantification of the osmotic potential of **(C)** Col-0, *canar-3,* and *canar-3 irk*-4 roots grown on 0.2× MS and **(D)** *XVE>>CANAR-3xHA* roots grown on 1× MS with (EST^+, 3 days induction) or without β-estradiol (mock). The experiment was carried out four times. Five roots per biological replicate were used. The graphs show data from four biological replicates, and error bars represent SD. A one-way ANOVA compared marked datasets ($^{**}P < 0.01$ and $^{***}P < 0.001$). See also Supplemental Figure 7.

uptake into the roots and increasing turgor pressure. Conversely, lower sugar content reduces water uptake and decreases turgor pressure. As the assessment of turgor pressure is problematic and complicated for a number of reasons, we measured root osmotic potential as a proxy for estimating internal cell pressure. Consistent with our genetic and microscopic data, a more negative osmotic potential was found in the roots of the *canar-3 irk-4* double mutant compared to Col-0, whereas *XVE>>CANAR-3xHA* had a less negative osmotic potential after induction (Figure 5C and 5D). No difference was observed for the *canar-3* mutant, again likely reflecting its subtle phenotype. We hypothesize that the regulation of the content of osmotically active sugars in root cells governs the extent of water uptake, which affects their internal pressure and, thus, the observed changes in cell size.

DISCUSSION

Taken all of our results together, we propose that the CARMA–CANAR module acts as a novel osmoregulatory system controlling cell size in the stele in response to external osmolality. Our genetic, molecular, microscopy, and biophysical data suggest that CANAR activity regulates the shoot-to-root phloem transport of sugars, which influences internal pressure via cellular water uptake and thus cell size (Figure 6). Root vascular cells in *XVE>>CARMA/canar-3* transgenic lines have a higher content of osmotically active sugars, causing increased water uptake and larger cell size on hypotonic media. On hypertonic media, the higher sugar content is countered by the osmolality of the environment; hence, the cell size is not affected. In contrast, vascular cells in *carma-1/XVE>>CANAR* lines have a lower content of sugars, which leads to decreased water retention and, thus, smaller cell size on hypertonic media. This effect is absent in hypotonic media, where water can diffuse inside the cells to balance the osmolality difference.

CANAR is expressed in both X and protophloem and is upregulated by PM-permeative sugars in both domains. *CARMA* fine-tunes *CANAR* expression predominantly in protophloem, likely via modulation of sensitivity to sugars. Since the *CARMA* and *CANAR* expression responses to sugar are similar (Figure 4D and 4E), it seems *CARMA* creates a feedback loop to establish

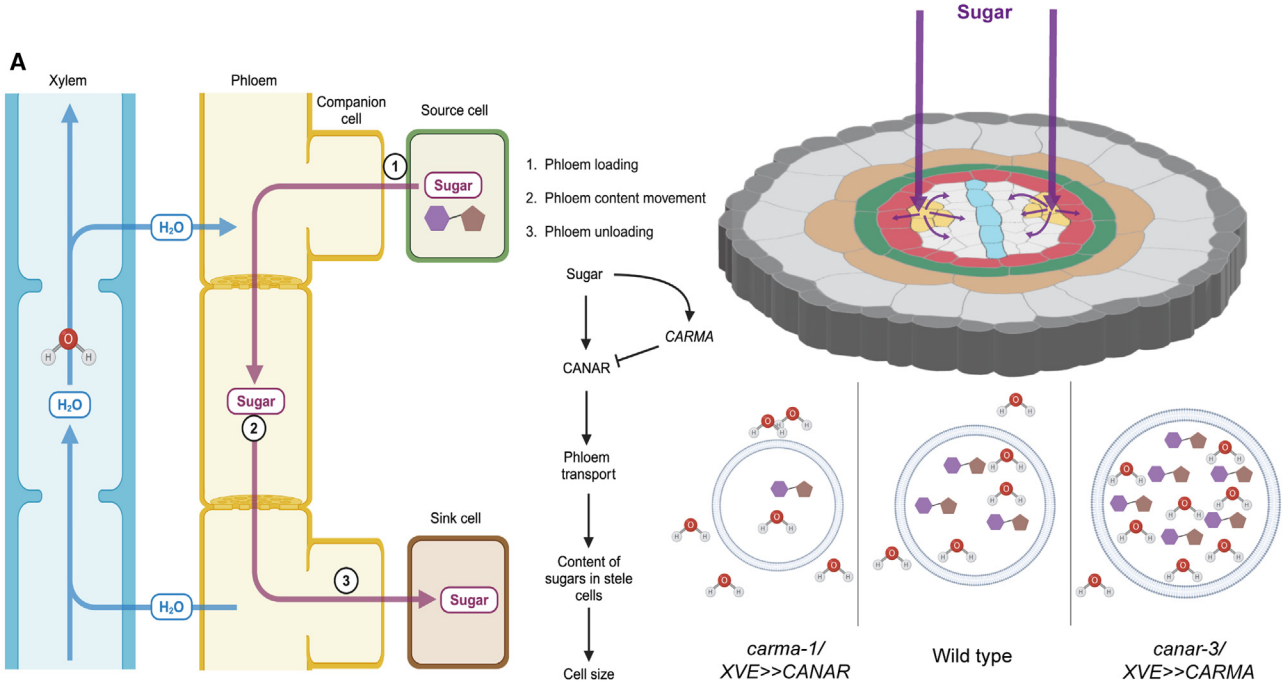

Figure 6. Graphical illustration of the CARMA–CANAR action.

The CARMA–CANAR module regulates phloem transport from shoot to roots. The availability of osmotically active compounds (mainly sugars) in stele cells determines water content and, thus, resultant cell size via internal pressure buildup. On hypotonic media, root stele cells in *XVE>>CARMA/canar-3* transgenic lines have a higher content of osmotically active sugars, leading to increased water uptake and larger cell size. On hypertonic media, the higher sugar content of stele cells is countered by the osmolality of the environment; hence, the cell size is not affected. In contrast, stele cells in *carma-1/XVE>>CANAR* lines have a lower content of sugars, which leads to decreased water retention and, thus, smaller cell size on hypertonic media. This effect is absent in hypotonic media, where water can diffuse inside the cells to balance the osmolality difference.

a differential of CANAR expression between the X and the protophloem. At this point, we are not certain why this differential is essential for cell adaptation to external osmolality.

The shoot-to-root transport of sugars consists of three steps: (1) phloem loading, (2) phloem movement, and (3) phloem unloading. Since we did not see any CFDA dye accumulation locked in root phloem in the tested transgenic lines (Figure 5A and 5B), the CARMA–CANAR function in step 3 can be excluded. Water exchange between X and phloem generates hydrostatic pressure differences between source and sink, driving the flow of the phloem content (Knoblauch et al., 2016; Hardtke, 2023). Taking into account the strong expression of CANAR in X, the CARMA–CANAR involvement in step 2 is conceivable. In any case, the identification of downstream targets of CANAR is required to obtain further mechanistic insight.

A link between subcellular sugar distribution and internal cell pressure was proposed previously (McGaughey et al., 2016), whereby the SWEETs and aquaporins in *Setaria viridis* guide sucrose and water partitioning between vacuoles, cytosol, and the storage parenchyma apoplast to adjust cell turgor. Our results indicate that CANAR modifies the expression of *SUCs* and *SWEETs*, but it is unclear whether this is a causal effect or compensatory mechanism due to an intricate system of sugar distribution, highlighting the central role of sugars in plant growth and development. For perspective, the *SWEET* family in *Arabidopsis* contains 20 genes, whereas animal genomes have only one (Julius et al., 2017). Moreover, the exact molecular function of sugar transporters in phloem loading/unloading is not entirely clear. Considering the causal effect, direct interaction is unlikely, given that CANAR is a PM-localized pseudokinase and influences the expression of both PM- and vacuolar-localized sugar transporters. Thus, it is more plausible that CANAR controls the regulator(s) of sugar transporter expression.

Our hypothesis about the osmoregulatory function of the CARMA–CANAR module may explain the extra endodermal divisions in the *irk-4* and *canar-3 irk-4* mutants and their absence in *canar-3* (Campos et al., 2020; Goff et al., 2023). Larger cells in the stele generate elevated mechanical pressure on the endodermis, the pressure-buffering tissue of the root (Hamant and Haswell, 2017). Both *canar-3* and *irk-4* plants have an enlarged stele area, although the increase is greater in *irk-4*. This suggests there is a certain pressure threshold after extra divisions in the endodermis are induced as a coping mechanism to dissipate the built-up mechanical pressure in the stele. This hypothesis is corroborated by the *canar-3 irk-4* double mutant, in which the stele area was more enlarged than in the single mutants, resulting in a higher incidence of extra endodermal divisions compared to *irk-4* (Goff et al., 2023). In line with our hypothesis, a cellulose-deficient *korrigan-1* mutant displayed root thickness twice that of the WT (Mielke et al., 2021). The enlargement resulted mostly from cortex cells. Swollen cortex cells generated mechanical pressure toward the outer epidermal cells and cells of inner tissues. Still, mechanical stress, as evidenced by elevated jasmonate signaling, was

observed only in endodermal and pericycle cells. The authors reasoned that epidermal cells dissipated the excessive pressure by expanding outward into the rhizosphere, and therefore, no extra cell divisions were induced in the endodermis.

The observations that *IRK* mutant (Campos et al., 2020), *CARMA* (Figure 2A–2D), and *CANAR* (Hajný et al., 2020) mutant/overexpressing lines exhibit defects in leaf vascular patterning suggest that stele area and leaf vein patterning (mediated via auxin canalization) are likely developmentally codependent. It is possible that an appropriate stele area is required for undisturbed vascular patterning or that sugars are vital signaling molecules instructing auxin canalization and, thus, vasculature establishment. However, we cannot uncouple these two phenomena, as the vasculature in cotyledons is already established in the embryo. Both scenarios are plausible as mechanical signals (laser ablation) in the shoot meristem induce reorientation of the PIN1 auxin exporter (Heisler et al., 2010), and leaf vasculature still forms, although imperfectly when auxin directional transport is not functional (Verna et al., 2019). Perhaps the residual vein-patterning activity could be attributed to positional information determined by the sugar transport? Alternatively, SWEETs might transport auxin, as it was recently reported that *Arabidopsis* SWEET13/14 proteins can transport multiple forms of gibberellins (Kanno et al., 2016). This broad substrate specificity is also displayed by ABCB transporters, which contribute to directional auxin transport (Cho and Cho, 2013).

In addition to the energy value of sugars, they also serve as signaling molecules. An extensive sugar-auxin signaling interaction network was recently described (Mishra et al., 2022). For instance, high glucose levels increased PIN2-GFP accumulation at the PM, promoting basipetal auxin transport in *Arabidopsis* (Mishra et al., 2009) while compromising PIN1-GFP expression, reducing auxin concentration in the root tip (Yuan et al., 2014). Moreover, external sugar (glucose/sucrose) application facilitated the accumulation of auxin on the concave side of the apical hook and contributed to the maintenance of the apical hook in a closed state (Chen et al., 2024). Given the interaction of CANAR with PIN1 (Hajný et al., 2020), the CARMA–CANAR module could be involved in the intricate interplay between sugar and auxin.

Manipulation of sugar distribution in plants is an obvious strategy for agriculture. Increasing the sugar content in roots can, in addition to improving the nutritional value, also change plant susceptibility to drought, cold, and heat stress (Julius et al., 2017). However, progress is hindered by a lack of known molecular regulators of sugar transporters. To our knowledge, CANAR is the first receptor controlling sink-to-source sugar transport. Our work may provide key entry points into the understanding of the intricate regulation of sugar distribution.

METHODS

Plant materials and growth conditions

All *A. thaliana* lines were in the Col-0 background. The T-DNA insertional mutant of *carma-1* (SAIL_704_A04) was obtained from NASC and genotyped with the primers listed in Supplemental Table 2. *canar-3* (*pxc2-3*, SM_3_31635), *canar-3/pxc2-3 irk-4*, and *XVE>>CANAR-3xHA* were described previously (Goff et al., 2023). Transgenic line *canar-3xXVE>>CARMA* was generated by crossing. Seeds were sterilized with 70% ethanol for 5 min and then with 100% ethanol for another 5 min. The seeds were plated on 1% plant agar (pH 5.9; Duchefa) supplemented with 0.5× MS medium basal salts (Duchefa) without sugar unless otherwise indicated. Five-day-old seedlings were used for imaging (counting 5 days after placement in the Phytochamber). Transgenic lines with the β-estradiol-inducible promoter (*XVE*) were grown on 5 μM β-estradiol from germination unless otherwise indicated. Plates were sealed with 3M micropore tape. Seeds were stratified on plates at 4°C for 1–2 days before being placed in a Phytochamber (16 h light/8 h dark cycle at a constant temperature of 21°C, light intensity ∼700 foot-candles).

Cloning and plant transformation

The transcriptional reporter for *CANAR* (AT5G01890) was constructed by LR recombination of the 4.7 kb promoter in pENTR 5′-TOPO (Goff et al., 2023) with NLS-GFP-GUS and 285 bp of the *CANAR* 3′ UTR (*ter*) in pENTR2B (generated via Gibson assembly-NEBuilder Hifi DNA assembly Master Mix) into the pK7m24GW-FAST destination vector. The deletion of 157 bp of *CARMA* (until annotated 5′ UTR of *CANAR*) was performed by amplifying truncated *pCANAR* in pENTR 5′-TOPO with primers containing a SalI restriction site. The amplicon was cut with SalI for 30 min (FastDigest; Thermo), cleaned, and ligated overnight at 16°C (T4 DNA ligase; NEB). The same approach was used for the second deletion (353 bp) of the *CARMA* locus. All three versions, *pCANAR::NLS-GFP-GUS-ter*, *pCANAR_CARMAΔ::NLS-GFP-GUS-ter*, and *pCANAR_CARMAΔΔ::NLS-GFP-GUS-ter*, were transformed into *carma-1* (SAIL_704_A04). Transcriptional reporters for *CARMA* (AT5G00810) were constructed by inserting 1300 bp of the *CARMA* promoter into pDONRP4-P1R via BP reaction and inserting 4975 bp of the *CARMA* promoter into pENTR 5′-TOPO via Gibson assembly. pDONRP4-P1R was recombined into pMK7S*NFm14GW and pENTR 5′-TOPO with NLS-GFP-GUS in pENTR2B (NLS-GFP-GUS fragment was amplified from pMK7S*NFm14GW and inserted in pENTR2B via SalI restriction and subsequent ligation) into the pH7m24GW destination vector via the LR reaction. Translation reporters were constructed using Invitrogen Multisite Gateway technology. *pCANAR* (in pENTR 5′-TOPO) and *pCVP2-XVE* (in pDONRP4-P1R) were recombined with *CANAR* (genomic fragment without stop codon in pENTR-D-TOPO) (Goff et al., 2023) and with *GFP-ter* (GFP flanked by pkpapkpa linker at the N terminus and *CANAR* 285 bp 3′ UTR at the C terminus in pDONRP2r-P3) via LR reaction. For the generation of *XVE>>CARMA*, the genomic fragment of *CARMA* (AT5G00810) was amplified from Col-0 genomic DNA and recombined into the pDONRP221 entry vector via BP reaction. This was then recombined into the pMDC7 destination vector via LR reaction. All primers used are listed in Supplemental Table 2.

Plant transformation

Transgenic *A. thaliana* plants were generated by the floral dip method using *Agrobacterium tumefaciens* (strain GV3101). Ecotype Col-0 served as the WT background for all lines.

CRISPR-Cas9

The T-DNA construct was constructed by cloning the two Cas9 spacer sequences "TGGCATGGACATGGTTAATG" and "GTTG GATTCCTCCAAGGTCT" as annealed oligonucleotides into the Gateway-compatible vectors pEn-Sa-Chimera and pDe-Sa-Cas9 EC, which carries *Staphylococcus aureus* Cas9 under the control of an egg cell-specific promoter, as described previously (Rönspies et al., 2022). *A. thaliana* Columbia seeds were stratified overnight at 4°C and cultivated in a greenhouse under 16 h light/8 h dark conditions at 22°C on soil (1:1 mixture of Floraton 3 [Floragard] and vermiculite [2–3 mm, Deutsche Vermiculite Dämmstoff]). After 4–5 weeks of growth, the plants were transformed with the CRISPR-Cas construct via *Agrobacterium*-mediated floral dip transformation. The transformed plants were cultivated for another 4–5 weeks until seed set. T1 seeds were surface sterilized with 4% sodium hypochlorite and stratified overnight at 4°C. The stratified seeds were sown on germination medium (4.9 g l^{-1} MS medium, 10 g l^{-1} saccharose [pH 5.7] and 7.6 g l^{-1} plant agar) with phosphinotricin and cefotaxime in sterile culture. The plates were placed in a growth chamber at 22°C under 16 h light/8 h dark conditions for 2 weeks. T1 primary transformants were selected and then cultivated in the greenhouse for 6–7 weeks until seed set. The T2 seeds were stratified and sown on germination medium without additives for 2 weeks. Afterward, the plants were screened for the presence of the deletion via PCR by combining the primers oMR765 "GAG ATGAAGTTGTTTCAGGGAGAC" and oMR766 "GGAGTCAA ATATGGGCCTGATATTC," spanning the deletion site, via bulk and individual plant screenings. For bulk screenings, one leaf each from 40 plants was cut off and the leaves were combined in one 1.5 ml reaction tube. For individual plant screenings, one leaf per plant was cut off and placed into a separate 1.5 ml reaction tube. The DNA extraction and screening were carried out as described previously (Rönspies et al., 2022). The presence of the deletions was confirmed by sequencing of the junctions by Eurofins Genomics. The software ApE (v.2.0.55) was used for alignment and analysis of the sequencing data. Of 200 screened plants, 3 tested positive for the deletion. Two of these lines (*canar-4 C2* and *C4*) were chosen for propagation and further analyses. The T3 offspring of these two lines were subjected to individual DNA extraction and screening to identify the individual plants harboring the deletion in the homozygous state. The plants were genotyped by PCR using primers specific for the deletion (oMR765/oMR766) as well as for the two WT junctions spanning the Cas9 cut sites (WT junction 1, oMR765/oMR792, GATTCTTGATCTCTCCGCCAAC; WT junction 2, oMR793, TATG TAATGTTAAATCCCTGTGCACC/oMR766). Homozygous plants were propagated in the greenhouse, and the seeds were harvested after 6–7 weeks.

RNA extraction, cDNA synthesis, and RT-qPCR analysis

Total RNA was isolated from seedlings for gene expression analysis in mutants and overexpressing lines or from roots for RNA sequencing using the Spectrum Plant Total R.N.A. Kit (Sigma). RNA was treated with TURBO DNase (Thermo) to avoid genomic DNA contamination. Three independent biological replicates were done per sample. For cDNA synthesis (RevertAid First Strand cDNA Synthesis kit, Thermo), 2 μg of total RNA was used with the Random Hexamer Primers mix (for RT-PCR of *CARMA* in Figure 1D) or with oligo(dT) for the rest of the RT-qPCRs. The generated cDNA was analyzed on the StepOnePlus Real-Time PCR system (Life Technologies) with gb SG PCR Master Mix (Generi Biotech) according to the manufacturer's instructions. The relative expression was normalized to *SERINE/THREONINE PROTEIN PHOSPHATASE*, *PP2A (AT1G69960)*. Three technical replicates were performed. All primers used are listed in Supplemental Table 2.

Confocal microscopy

Five-day-old roots were stained with propidium iodide (PI) (10 μg/ml) and visualized via laser scanning confocal microscopy using a Zeiss LSM900 with a 40× water immersion objective. Fluorescent signals were visualized as PI (excitation 536 nm, emission 585–660 nm) and eGFP (excitation 488 nm, emission 492–530 nm). For stele area analysis, z stacks of approximately 100 μm were taken. ImageJ software was used for image post-processing and quantification of stele area.

Histological analyses

β-glucuronidase staining was performed as described in Prát et al. (2018). The staining reaction was stopped with 70% ethanol and left for 2 days to remove chlorophyll. Seedlings were mounted in chloral hydrate and examined using a stereomicroscope (Olympus). ClearSee tissue clearing (Kurihara et al., 2015) was performed to count the cells in the transverse optical sections. The seedlings were fixed in 4% paraformaldehyde in PBS (1 h in vacuum), washed with PBS, and placed into ClearSee solution (25% urea, 15% sodium deoxylate, and 10% xylitol) for at least 3 days. Then, the seedlings were transferred into 0.1% Calcofluor white in ClearSee solution for 60 min, followed by a wash with ClearSee solution for 30 min, and then mounted on slides with ClearSee. Two-sided tape was used on slides to prevent tissue disruption.

Stele area and vascular cell number quantification

z stacks of ∼100 μm (1-μm-thick slices) capturing the root meristematic zone were acquired. The bleach correction plugin in ImageJ was applied to all images to compensate for decreasing PI signal in the deeper part of the root. The stele area and the number of vascular cells were assessed in the transverse sections located ∼100 μm above the quiescent center using ImageJ.

Quantification of *pCANAR* expression in protophloem

z stacks of approximately 100 μm capturing the root meristematic zone were acquired. Multiple transverse sections with nuclear GFP fluorescence in X and protophloem in the same plane were taken for each z stack. The fluorescent signal in the protophloem was normalized to the X signal in each transverse section, and the average value of all sections from one root was calculated and plotted into a graph.

Software

Postprocessing of confocal images was done in ImageJ (https://imagej.nih.gov/ij/). Figures were generated in Adobe Illustrator or Biorender. Graphs and statistics were completed in GraphPad Prism 9.

5′ and 3′ RACE experiments

The 5′ RACE sequencing library was generated from 5-day-old roots with template-switching RT following the protocol outlined in Montez et al. (2023). Briefly, 500 ng of total RNA, post DNase treatment, served as the template for cDNA generation using SuperScript II. The resulting cDNA was purified using AMPure XP magnetic beads (Beckman Coulter) and amplified in a series of three PCRs with specific primers (first PCR, only TSO_n1; second PCR, TSO_n2 and CARMA_5RACE; third PCR, Illumina indexing primers) and Phusion polymerase. Following quality checks, the final PCR product was sequenced using Illumina MiSeq.

The 3′ RACE sequencing was completed based on the procedure described by Warkocki et al. (2018) with ligation of the preadenylated adaptor to the 3′ end of the RNA using truncated T4 RNA ligase 2. RNA ligated with the RA3_15N adaptor (containing UMI) was cleaned on AMPure XP magnetic beads and subjected to RT reaction with SuperScrit III. After three rounds of PCR with specific primers (first PCR, CARMA_3RACE and RTPXT; second PCR, mXTf and mXTr; third PCR, Illumina indexing primers) and cleaning each PCR on AMPure beads, prepared libraries were sequenced using Illumina MiSeq.

Sequence reads were trimmed to remove adapter sequences using cutadapt (v.1.18; Martin, 2011). STAR (v.2.7.8a; Dobin et al., 2013) was utilized to align the reads to the reference genome, followed by UMI-based filtering using UMI-tools (v.1.1.0; Smith et al., 2017). The position of the read end nucleotide was extracted using bedtools (v.2.30.0; Quinlan and Hall, 2010). All primers used are listed in Supplemental Table 2.

CFDA staining

CFDA (Sigma-Aldrich, CAS: 79955-27-4) was diluted in DMSO to create 10 mM stock. Shoots of 5-day-old seedlings were placed on a glass cover lid, and 2 μl of working 1 mM solution in water was placed on one leaf. After 45 min, the seedlings were placed into a chamber with an agar block stained with PI and imaged using confocal microscopy in a GFP channel (excitation 488 nm, emission 492–530 nm).

Root osmotic potential

Root osmotic potential (ψs) was measured using C-52 thermocouple psychrometric chambers and an HR-33T Dew Point Microvoltmeter (Wescor, USA) in dew point mode (Campbell et al., 1973; Briscoe, 1986). Prior to ψs measurement, root samples were subjected to a freeze–thaw cycle and equilibrated for 40 min after insertion into the chamber. Each sample consisted of roots from five seedlings. The chambers were calibrated with NaCl solutions of different osmolality.

Osmolality measurement

An Osmometer 3320 (Advanced Instruments) was used for measuring liquid medium osmolality according to the manufacturer's instructions. The machine was calibrated using calibration standards at 50, 850, and 2000 mOsm/kg. A sampler tip was inserted into the sampler and 20 μl of sample was loaded. The sample was visually inspected to avoid any bubbles, and any excess solution on the sampler tip was removed using soft, no-lint, non-ionic paper tissue. The osmometer chamber was cleaned, and the sample was inserted to measure osmolality values. All tested liquid media were mixed for 30 min on a magnetic stirrer to ensure complete dissolution of all substances. The media were measured at room temperature.

FUNDING

The work of J.H. was supported by the EMBO long-term fellowship (ALTF 217-2021) and by the project JG_2024_003 implemented within the Palacký University Young Researcher Grant. The work of R.M.I.K.R. and J.M.v.N. is supported by NSF CAREER award 1751385.

ACKNOWLEDGMENTS

No conflict of interest is declared.

AUTHOR CONTRIBUTIONS

Conceptualization, J.H.; funding, J.H. and O.N.; writing, editing, and interpretation of data, J.H., S. Sacharowski, S. Swiezewski, A.P., J.M.v.N., D.Z., C.S.H., and R.M.I.K.R.; methodology, J.H., D.Z., S. Sacharowski, T.T., and R.M.I.K.R.; RACE experiments, S. Sacharowski and S. Swiezewski; bioinformatics, M.K.; microscopy, J.H. and R.M.I.K.R.; cloning, J.H., D.Z., and T.T.; generation of transgenic lines, J.H. and T.T.; CRISPR-Cas9, M.R. and H.P.; psychrometry, M.Š.

SUPPLEMENTAL INFORMATION

Supplemental information is available at *Molecular Plant Online*.

Received: July 8, 2024
Revised: September 10, 2024
Accepted: September 26, 2024
Published: September 30, 2024

REFERENCES

Ali, O., Cheddadi, I., Landrein, B., and Long, Y. (2023). Revisiting the relationship between turgor pressure and plant cell growth. New Phytol. **238**:62–69.

Bavnhøj, L., Driller, J.H., Zuzic, L., Stange, A.D., Schiøtt, B., and Pedersen, B.P. (2023). Structure and sucrose binding mechanism of the plant SUC1 sucrose transporter. Nat. Plants **9**:938–950.

Briscoe, R. (1986). Thermocouple Psychrometers for Water Potential Measurements. In Advanced Agricultural Instrumentation: Design and Use, W.G. Gensler, ed. (Springer Netherlands), pp. 193–209.

Campbell, E.C., Campbell, G.S., and Barlow, W.K. (1973). A dewpoint hygrometer for water potential measurement. Agric. Meteorol. **12**:113–121.

Campos, R., Goff, J., Rodriguez-Furlan, C., and Van Norman, J.M. (2020). The Arabidopsis Receptor Kinase IRK Is Polarized and Represses Specific Cell Divisions in Roots. Dev. Cell **52**:183–195.e4.

Chen, J., Yang, L., Zhang, H., Ruan, J., and Wang, Y. (2024). Role of sugars in the apical hook development of Arabidopsis etiolated seedlings. Plant Cell Rep. **43**:131.

Cho, M., and Cho, H.T. (2013). The function of ABCB transporters in auxin transport. Plant Signal. Behav. **8**:e22990.

Chorostecki, U., Bologna, N.G., and Ariel, F. (2023). The plant noncoding transcriptome: a versatile environmental sensor. EMBO J. **42**:e114400.

Cosgrove, D.J. (2016). Plant cell wall extensibility: connecting plant cell growth with cell wall structure, mechanics, and the action of wall-modifying enzymes. J. Exp. Bot. **67**:463–476.

Dobin, A., Davis, C.A., Schlesinger, F., Drenkow, J., Zaleski, C., Jha, S., Batut, P., Chaisson, M., and Gingeras, T.R. (2013). Gingeras TR. STAR: ultrafast universal RNA-seq aligner. Bioinformatics **29**:15–21.

Durand, M., Mainson, D., Porcheron, B., Maurousset, L., Lemoine, R., and Pourtau, N. (2018). Carbon source–sink relationship in Arabidopsis thaliana: the role of sucrose transporters. Planta **247**:587–611.

Fandino, A.C.A., Jelinkova, A., Marhava, P., Petrasek, J., and Hardtke, C.S. (2023). Ectopic assembly of an auxin efflux control machinery shifts developmental trajectories Advance Access, published September 17, 2023. https://doi.org/10.1101/2023.09.16.558043.

Fukuda, H., and Ohashi-Ito, K. (2019). Vascular tissue development in plants. Curr. Top. Dev. Biol. **131**:141–160.

Geiger, D. (2020). Plant glucose transporter structure and function. Pflugers Arch. **472**:1111–1128.

Goff, J., Rony, R.M.I.K., Ge, Z., Hajný, J., Rodriguez-Furlan, C., Friml, J., and Norman, J.M.V. (2023). PXC2, a polarized receptor kinase, functions to repress ground tissue cell divisions and restrict stele size Advance Access published March 19. bioRxiv. https://doi.org/10.1101/2021.02.11.429611.

Guo, W.-J., Nagy, R., Chen, H.-Y., Pfrunder, S., Yu, Y.-C., Santelia, D., Frommer, W.B., and Martinoia, E. (2014). SWEET17, a Facilitative Transporter, Mediates Fructose Transport across the Tonoplast of Arabidopsis Roots and Leaves. Plant Physiol. **164**:777–789.

Hajný, J., Prát, T., Rydza, N., Rodriguez, L., Tan, S., Verstraeten, I., Domjan, D., Mazur, E., Smakowska-Luzan, E., Smet, W., et al. (2020). Receptor kinase module targets PIN-dependent auxin transport during canalization. Science **370**:550–557.

Hamant, O., and Haswell, E.S. (2017). Life behind the wall: sensing mechanical cues in plants. BMC Biol. **15**:59.

Hardtke, C.S. (2023). Phloem development. New Phytol. **239**:852–867.

Heisler, M.G., Hamant, O., Krupinski, P., Uyttewaal, M., Ohno, C., Jönsson, H., Traas, J., and Meyerowitz, E.M. (2010). Alignment between PIN1 Polarity and Microtubule Orientation in the Shoot Apical Meristem Reveals a Tight Coupling between Morphogenesis and Auxin Transport. PLoS Biol. **8**:e1000516.

Hohl, M., and Schopfer, P. (1991). Water Relations of Growing Maize Coleoptiles 1. Plant Physiol. **95**:716–722.

Julius, B.T., Leach, K.A., Tran, T.M., Mertz, R.A., and Braun, D.M. (2017). Sugar Transporters in Plants: New Insights and Discoveries. Plant Cell Physiol. **58**:1442–1460.

Kanno, Y., Oikawa, T., Chiba, Y., Ishimaru, Y., Shimizu, T., Sano, N., Koshiba, T., Kamiya, Y., Ueda, M., and Seo, M. (2016). AtSWEET13 and AtSWEET14 regulate gibberellin-mediated physiological processes. Nat. Commun. **7**:13245.

Knoblauch, M., Knoblauch, J., Mullendore, D.L., Savage, J.A., Babst, B.A., Beecher, S.D., Dodgen, A.C., Jensen, K.H., and Holbrook, N.M. (2016). Testing the Münch hypothesis of long distance phloem transport in plants. Elife **5**:e15341.

Kurihara, D., Mizuta, Y., Sato, Y., and Higashiyama, T. (2015). ClearSee: a rapid optical clearing reagent for whole-plant fluorescence imaging. Development **142**:4168–4179.

Le Hir, R., Spinner, L., Klemens, P.A.W., Chakraborti, D., de Marco, F., Vilaine, F., Wolff, N., Lemoine, R., Porcheron, B., Géry, C., et al. (2015). Disruption of the Sugar Transporters AtSWEET11 and AtSWEET12 Affects Vascular Development and Freezing Tolerance in Arabidopsis. Mol. Plant **8**:1687–1690.

Martin, M. (2011). Cutadapt removes adapter sequences from high-throughput sequencing reads. EMBnet J **17**:10–12.

McGaughey, S.A., Osborn, H.L., Chen, L., Pegler, J.L., Tyerman, S.D., Furbank, R.T., Byrt, C.S., and Grof, C.P.L. (2016). Roles of Aquaporins in Setaria viridis Stem Development and Sugar Storage. Front. Plant Sci. **7**:1815.

Mielke, S., Zimmer, M., Meena, M.K., Dreos, R., Stellmach, H., Hause, B., Voiniciuc, C., and Gasperini, D. (2021). Jasmonate biosynthesis arising from altered cell walls is prompted by turgor-driven mechanical compression. Sci. Adv. **7**:eabf0356.

Mishra, B.S., Singh, M., Aggrawal, P., and Laxmi, A. (2009). Glucose and Auxin Signaling Interaction in Controlling Arabidopsis thaliana Seedlings Root Growth and Development. PLoS One **4**:e4502.

Mishra, B.S., Sharma, M., and Laxmi, A. (2022). Role of sugar and auxin crosstalk in plant growth and development. Physiol. Plant. **174**:e13546.

Montez, M., Majchrowska, M., Krzyszton, M., Bokota, G., Sacharowski, S., Wrona, M., Yatusevich, R., Massana, F., Plewczynski, D., and Swiezewski, S. (2023). Promoter-pervasive transcription causes RNA polymerase II pausing to boost DOG1 expression in response to salt. EMBO J **42**:e112443.

Prát, T., Hajný, J., Grunewald, W., Vasileva, M., Molnár, G., Tejos, R., Schmid, M., Sauer, M., and Friml, J. (2018). WRKY23 is a component of the transcriptional network mediating auxin feedback on PIN polarity. PLoS Genet. **14**:e1007177.

Quinlan, A.R., and Hall, I.M. (2010). BEDTools: a flexible suite of utilities for comparing genomic features. Bioinformatics **26**:841–842.

Rönspies, M., Schindele, P., Wetzel, R., and Puchta, H. (2022). CRISPR–Cas9-mediated chromosome engineering in Arabidopsis thaliana. Nat. Protoc. **17**:1332–1358.

Ross-Elliott, T.J., Jensen, K.H., Haaning, K.S., Wager, B.M., Knoblauch, J., Howell, A.H., Mullendore, D.L., Monteith, A.G., Paultre, D., Yan, D., et al. (2017). Phloem unloading in Arabidopsis roots is convective and regulated by the phloem-pole pericycle. Elife **6**:e24125.

Scarpella, E., Marcos, D., Friml, J., and Berleth, T. (2006). Control of leaf vascular patterning by polar auxin transport. Genes Dev. **20**:1015–1027.

Smith, T., Heger, A., and Sudbery, I. (2017). UMI-tools: modeling sequencing errors in Unique Molecular Identifiers to improve quantification accuracy. Genome Res **27**:491–499.

Verna, C., Ravichandran, S.J., Sawchuk, M.G., Linh, N.M., and Scarpella, E. (2019). Coordination of tissue cell polarity by auxin transport and signaling. Elife **8**:e51061.

Wang, K.C., and Chang, H.Y. (2011). Molecular Mechanisms of Long Noncoding RNAs. Mol. Cell **43**:904–914.

Wang, J., Kucukoglu, M., Zhang, L., Chen, P., Decker, D., Nilsson, O., Jones, B., Sandberg, G., and Zheng, B. (2013). The Arabidopsis LRR-RLK, PXC1, is a regulator of secondary wall formation correlated with the TDIF-PXY/TDR-WOX4 signaling pathway. BMC Plant Biol. **13**:94.

Warkocki, Z., Krawczyk, P.S., Adamska, D., Bijata, K., Garcia-Perez, J.L., and Dziembowski, A. (2018). Uridylation by TUT4/7 restricts retrotransposition of human LINE-1s. Cell **174**:1537–1548.e29.

Xue, X., Wang, J., Shukla, D., Cheung, L.S., and Chen, L.-Q. (2022). When SWEETs Turn Tweens: Updates and Perspectives. Annu. Rev. Plant Biol. **73**:379–403.

Yuan, T.-T., Xu, H.-H., Zhang, K.-X., Guo, T.-T., and Lu, Y.-T. (2014). Glucose inhibits root meristem growth via ABA INSENSITIVE 5, which represses PIN1 accumulation and auxin activity in Arabidopsis. Plant Cell Environ. **37**:1338–1350.

Zuo, J., Niu, Q.-W., and Chua, N.-H. (2000). An estrogen receptor-based transactivator XVE mediates highly inducible gene expression in transgenic plants. Plant J. **24**:265–273.